Materiales de Construcción 75 (359)
July-September 2025, e385
ISSN-L: 0465-2746
https://doi.org/10.3989/mc.2025.387524

The phase composition and microstructure development of a construction composite made from sewage sludge and biomass ash

V. Zalar Serjun[a], S. Dolenec[a,b], M. Dolenec[b], A. Mladenović[a], P. Pavšič[a] ✉

a. Slovenian National Building and Civil Engineering Institute, (Ljubljana, Slovenia)
b. University of Ljubljana, Faculty of Natural Sciences and Engineering, (Ljubljana, Slovenia)
✉: primoz.pavsic@zag.si

Received 13 June 2024
Accepted 8 February 2025
Available on line 11 March 2026

ABSTRACT: Waste from one industry can often serve as raw material for another. Previous research has shown that sewage sludge stabilized with biomass ash can form a construction composite with "Controlled Low-Strength Material" properties. This study focuses on the microstructural properties of such composites over time, investigating changes in phase composition and pore size distribution, as well as susceptibility to carbonation. Techniques such as X-ray powder diffraction, Fourier transformation infrared spectroscopy, scanning electron microscopy with energy dispersive spectroscopy, mercury porosimetry, and nitrogen gas sorption were employed. Results indicated that ash, a fine-grained, calcium-rich material, promotes new phase formation when combined with sewage sludge. Over time, common hydration phases like C-A-H and C-(A-)S-H were identified. The research demonstrated a direct correlation between microstructure development and phase evolution in the construction composite.

KEY WORDS: Construction composite; Sewage sludge; Biomass ash; Microstructure; Phase analysis.

Citation/Citar como: Zalar Serjun V, Dolenec S, Dolenec M, Mladenović A, Pavšič P. 2025. The phase composition and microstructure development of a construction composite made from sewage sludge and biomass ash. Mater. Construcc. 75(359):e385. https://doi.org/10.3989/mc.2025.387524

RESUMEN: *Composición de las fases y desarrollo microestructural de un material de construcción compuesto con lodos de depuradora y cenizas de biomasa.* Los residuos de una industria pueden servir usualmente como materia prima para otra industria. Investigaciones anteriores han demostrado que los lodos de depuradora estabilizados con cenizas de biomasa pueden formar un material compuesto de construcción con propiedades de «material de baja resistencia controlada». Este estudio se centra en las propiedades microestructurales de tales compuestos a lo largo del tiempo, investigando los cambios en la composición de las fases y la distribución del tamaño de los poros, así como la susceptibilidad a la carbonatación. Se emplearon técnicas como la difracción de rayos X en polvo, la espectroscopia infrarroja por transformación de Fourier, la microscopia electrónica de barrido con espectroscopia de energía dispersiva, la porosimetría de mercurio y la sorción de gas nitrógeno. Los resultados indicaron que la ceniza, un material de grano fino y rico en calcio, promueve la formación de nuevas fases cuando se combina con lodos de depuradora. Con el tiempo, se identificaron fases de hidratación comunes como C-A-H y C-(A-)S-H. La investigación demostró una correlación directa entre el desarrollo de la microestructura y la evolución de las fases en el compuesto de construcción.

PALABRAS CLAVE: Materiales compuestos de construcción; Lodos de depuradora; Cenizas de biomasa; Microestructura; Análisis de fases.

1. INTRODUCTION

The handling of sewage sludge, a residue from wastewater treatment, is of great importance in Europe. The volume of sewage sludge generated in the European Union (EU) is significant, with conflicting reports suggesting it could be anywhere between 3 and 16 million tons of dry matter per year (1). Due to the expansion of wastewater collection and treatment systems, as well as the implementation of stricter environmental quality standards, the amount of sewage sludge generated annually is continually increasing (2, 3). In most EU countries, the disposal of sewage sludge in landfills has gradually decreased, with an increasing trend towards the use of treated sludge as a soil conditioner or biofuel. Due to strict guidelines concerning agricultural soil quality and crop production, and the significant associated energy requirements, however, these options are not always applicable, meaning there is an imperative need for alternative methods to manage sewage sludge (4, 5). The first choice in many EU countries is still the direct application of sewage sludge in agriculture, with the second most commonly-used method being composting (6). According to EUROSTAT 2022 (7), up to 26% of sewage sludge in the EU is used in agriculture, while composting accounts for an additional 18%. The amount of sewage sludge used in agriculture and for composting varies considerably between EU countries, ranging from zero in Malta and the Netherlands to almost 100% in Ireland. In Ireland, Spain, Estonia, Bulgaria and the Czech Republic more than 50% of sewage sludge generated is used in agriculture, while composting is more common in Finland, Lithuania, Slovakia, Cyprus and Hungary. Malta relies exclusively on landfilling to dispose of sewage sludge, while incineration is predominant in the Netherlands, Belgium, Germany and Austria. Alternative disposal methods are more common in Slovenia, Croatia and Poland (8, 9). In Slovenia, relatively large quantities of sewage sludge are processed together with biomass ash from the pulp and paper industry to produce construction composites. Combining these two waste materials represent great synergistic effects, as it creates a solution for bio-ash waste, which, now generated in increasing quantities, has also become a cause for concern.

The pulp and paper industry is an important industrial sector that generates significant amounts of lignocellulosic waste. In Europe, this sector generates 11 million tons of waste annually, of which 70% comes from the production of deinked recycled paper (10, 11). Deinking paper sludge is a waste or by-product of the paper deinking process and accounted for 4.8 to 9.7 million tons (dry matter) of waste in 2019 alone (12). As paper is one of the most recycled materials worldwide, and the recycling rate in Europe has already reached 72.5%, significant amounts of deinking paper sludge have been generated and will continue to be generated (11-13). The amount of deinking paper sludge generated during the recycling of waste paper varies between 20 % (for newsprint) and 40 % (for tissue paper) (12). According to the Waste Directive (for prevention and reuse), the current management of this waste, which primarily involves incineration or landfilling, is far from ideal (12, 14). With the aim of using residues as renewable fuels for energy recovery in the pulp and paper industry, deinking paper sludges are often incinerated at temperatures between 800 and 900°C. As a result of this process, a significant amount of biomass ash is produced as a by-product or waste (15, 16). This ash contains various fillers, pigments and coagulants, with its composition influenced by the production process. Furthermore, the technology and temperature of the boilers used during the combustion process can also influence the properties of the resulting ash (16, 17). Biomass ash can be used for various purposes e.g. in civil engineering and the cement industry, or for water treatment, soil stabilization, and the immobilization of pollutants, as well as in some other areas (14, 18, 19).

The EU has prioritized a transition to a more circular economy, with the aim of promoting the sustainable use of resources. This includes implementing policies that help “close the loop” of the product life cycle, by increasing recycling and reuse. Such efforts not only benefit the environment, but also have a positive impact on the economy (20). This plan aims to extract the maximum value and benefit from all raw materials, products and waste, promote energy savings and reduce greenhouse gas emissions. The proposals cover the entire life cycle of a material, including waste management and the market for secondary raw materials. Following this concept of creating a synergistic effect across different sectors i.e. waste management and the construction industry, as well as the EU waste hierarchy, some research has already been conducted investigating the application of sewage sludge mixed with biomass ash or other types of ash for construction (18, 19, 21, 22). The results of this research show that liquid sewage sludge can be successfully stabilized in order to produce stable structural composites that are both technically and ecologically acceptable.

Since the material properties are determined by the microstructure, which in turn depends on the composition and processing of the material, comprehensive knowledge of the microstructure of these composites is crucial (9, 18, 19, 23, 24). There are no detailed studies of construction materials made from sewage sludge enriched with biomass ash known in the literature.

In an attempt to investigate the type of microstructure responsible for the positive properties of the building material produced from biomass ash-enriched sewage sludge (19), this study pursues two interrelated objectives; namely, the development of phases and porosity was investigated as a function of time, and the susceptibility of the material to

carbonation was analysed. In order to promote alternative options for the use of liquid sewage sludge and paper ash, it is essential to understand the mechanism of microstructure evolution in the composite material being investigated. This research addresses the challenges outlined within the theme "Secondary Raw Materials" in the Strategic Implementation Plan (SIP) of the European Innovation Partnership on Raw Materials, by identifying and developing more sustainable downstream uses for two environmentally-challenging types of waste.

2. MATERIALS AND METHODS

Sewage sludge and biomass ash, both obtained from the VIPAP Videm Krško d.d. paper mill in Slovenia, were used in this study as raw materials for the production of composites.

The sewage sludge was produced through the aerobic biological treatment of industrial and municipal wastewater. Sludge samples with about 1% dry matter (to a total volume of 100 l) were taken from the aeration tank before dewatering. Biomass ash was produced in a steam boiler during the incineration of a mixture of deinking fibre paper sludge, waste wood and bark. The ash consisted of about 90% (by weight) bottom ash and 10% (by weight) fly ash. The paper ash used in this study has been previously approved as a construction material due to Slovenian technical approval (18). The biomass ash (approx. 100 kg in total) was removed from a silo according to the procedure prescribed in EN 14899.

The sewage sludge-biomass ash composite was prepared and cured according to a procedure established previously (19). The raw components were mixed in a laboratory planetary mixer (EN 196-1) at a 1:1 mass ratio. Twenty-one cubic test specimens (sized 150 mm ×150 mm ×150 mm) were produced according to EN 12390-2 using a vibrating table. The specimens were removed from the mould after 2 days then cured in a sealed container at a temperature of 23 ºC ± 2 ºC and a relative humidity of at least 98%. The specimens were then sampled at different time intervals, namely after 3, 7, 14, 28, 56 and 90 days. To investigate the effect of the carbonation potential of the composite, after 90 days 3 samples were cured for a further 28 days under laboratory conditions (45-60 % RH and 23 °C ± 2 ºC) (see Table 1).

Table 1. Designations of the samples.

Curing period	3 days	7 days	14 days	28 days	56 days	90 days	90 + 28 days
Designation	3 D	7 D	14 D	28 D	56 D	90 D	KARB

In order to characterise the composition and microstructure of the composite, material was extracted from the samples 3 D, 7 D, 14 D, 28 D, 56 D and 90 D by carefully breaking the cubes with a chisel so as to obtain a central portion of each sample. The KARB sample was taken across a profile, extending from the surface of the cubic samples to a depth of 1.5 cm below the surface (corresponding to the carbonated area, according to the phenolphthalein test; Figure 1) The chemical and microstructural compositions of the sewage sludge and biomass ash were determined by X-ray fluorescence, X-ray powder diffraction analysis (XRD), Fourier transform infrared spectroscopy (FTIR) and scanning electron microscopy with energy dispersive spectroscopy (SEM/EDS). In order to carry out mineralogical characterization and chemical analysis, the sewage sludge was first dried to a constant mass at 40 °C, to prevent potential phase transformations.

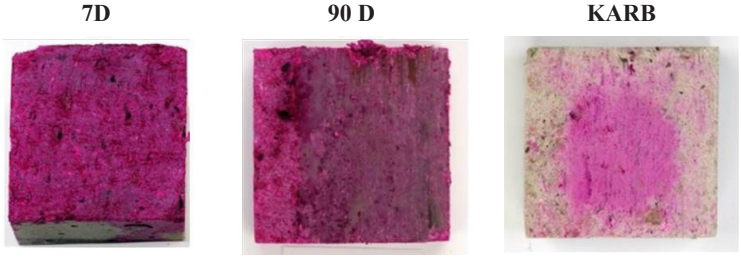

Figure 1. The result of phenolphthalein indicator tests for 7D, 90D and KARB sample.

The chemical compositions of the sewage sludge and biomass ash were determined by a Thermo Scientific ARL PERFORM'X Wavelength Dispersive X-Ray Fluorescence Spectrometer (WD XRF) fitted with a Rh-Target X-ray tube using the UniQuant programme. Before conducting the measurements, a fused bead was prepared by heating a mixture of the sample and flux (50 % lithium tetraborate/ 50 % lithium metaborate) in a ratio of 1:10 to 1025 °C. The loss on ignition (LOI) was analysed in accordance with EN 196-2. Additionally, the chloride content of the raw materials was determined in accordance with EN 196-2 (point 4.5.16).

Phase analysis of raw materials and composites was performed by X-ray powder diffraction using a Philips PW3710 diffractometer equipped with Cu $K\alpha_1$ radiation, a secondary graphite monochromator and an automatic divergence slit. Powder diffraction data were collected at a tube voltage of 40 kV and a tube current of 30 mA in the range from 8 ° to 70 °2θ, using a step size of 0.01 °2θ and a measurement time of 0.5 seconds per step. All samples were analysed using the HighScore (Plus) software package (version 4.1, 2014) (PANalytical B.V., Almelo, The Netherlands) and the PDF-4+ (2016) database (Pennsylvania, USA). Quantitative phase analysis (QPA) followed the Rietveld full-pattern fit method utilizing the internal standard approach, with the addition of 15 wt% of the pure crystalline corundum standard reference material SRM NIST-676a to all samples. The resulting standard-sample mixtures were then homogenised in a MillMax 20 ball mill at 25 Hz for 5 minutes. Systematic measurement errors (angular aberrations, sample transparency or displacement, X-ray optical effects and so on) were corrected based on the known positions and intensities of the standard (NIST-676a) for each sample individually (25). The measured profile and a profile calculated from crystal structure of the phases data were compared. Once we added an internal standard to the sample, the overestimation of this phase (and thus of all other crystalline phases) was corrected for determine the amount of amorphous material. Quality of calculated profile with smaller differences to the measurement was proven by the agreement indices GOF (goodness of fit, the ratio between the weighted and expected profile R-factors).

The raw materials and composites were analyzed by Fourier transform infrared spectroscopy (FTIR) using a Spectrum 100 spectrometer from Perkin Elmer (Connecticut, USA). Thirty-two signal-averaged scans of the samples were acquired. Three measurements were taken per sample in each measurement period. Powder pellets (three per sample) were pressed from samples mixed with KBr at a ratio of approximately 1:200. FTIR spectra were recorded at a spectral resolution of 4 cm^{-1} in the range from 4000 to 370 cm^{-1}. The average band area and band height were calculated for specific FTIR absorption bands (I, II, XVI, XVII and XXI), as shown in Figure 2. The program Spectra Manager (version 2.13.00) was used for baseline correction and normalization of the FTIR spectra. For baseline correction, the raw spectra were pre-processed using a simple linear two-point subtraction method. The spectra were then vector normalized. The average band height and band area of the FTIR absorption bands selected were calculated using the two-point basis method. In the case of the XVI and XVII bands, a deconvolution with a FWHM value (full width at half maximum of the expected Lorenz waveform) of 150 was additionally applied to the spectra.

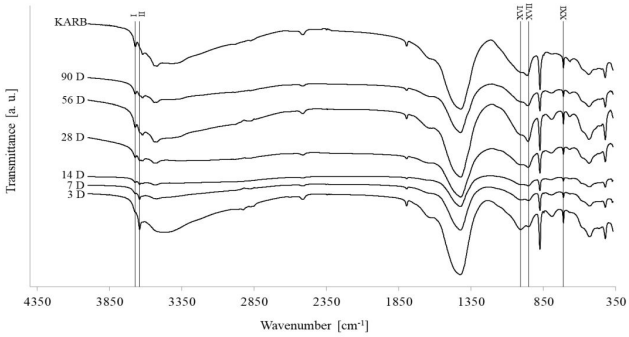

Figure 2. FTIR spectra of the sewage sludge-biomass ash composites at different hydration periods, with the FTIR absorption bands considered for peak height and peak area calculations indicated.

The composition and microstructural features of the samples were investigated by SEM/EDS on polished cross-sections using a JEOL 5500 LV microscope (Tokyo, Japan) equipped with energy dispersive X-ray spectroscopy (Oxford Instruments, UK). The low vacuum mode was employed for analysis, with a chamber pressure of 12 to 13 Pa and an accelerating voltage of 20 kV.

The hydration reaction of the composite was stopped via the solvent replacement procedure, using isopropanol and vacuum drying to a constant weight in a desiccator (26).

The porosity, total pore area, (average and median) pore size diameter and pore size distribution were all determined by mercury intrusion porosimetry (MIP), considering the Washburn equation and assuming a contact angle of 130°. All MIP measurements were performed using an AutoPore IV 9500 porosimeter (Micromeritics, Norcross, Georgia), in a pressure range up to 414 MPa. Additionally, the pore size distribution and Brunauer, Emmet and Teller (BET) surface areas of the composites were measured by nitrogen gas sorption using an ASAP2020 instrument, also from Micromeritics. The samples were degassed at 60°C, using an evacuation rate of 0.67 kPa/s until a final vacuum of 2 Pa was reached. The BET value and pore size distribution were determined using the Barret, Joyner and Halenda (BJH) method and the Halsey equation. To ensure accuracy of the measurements obtained, three specimens were taken from each cubic sample for both the MIP and nitrogen gas sorption analysis. The standard deviations of the pore size distribution measurements, calculated using both MIP and nitrogen gas sorption, are shown in Table 2.

Table 2. The maximum, minimum and average standard deviations of repeated pore size distribution measurements from each sample.

	Average standard deviations for each set of measurements	
	MIP (Log Differential Intrusion) (mL/g)	Nitrogen gas sorption (Pore Volume) ($cm^3/g \cdot nm$)
minimal	0.009	0.007
maximal	0.017	0.013
average	0.012	0.010

The results show very good repeatability with respect to both the MIP and gas sorption measurements.

3. RESULTS AND DISCUSSION

3.1. Characterization of the sewage sludge and biomass ash

The microstructural and morphological characteristics of the dried sewage sludge and biomass ash, as obtained by combination of XRD and SEM/EDS, are presented in Figure 3.

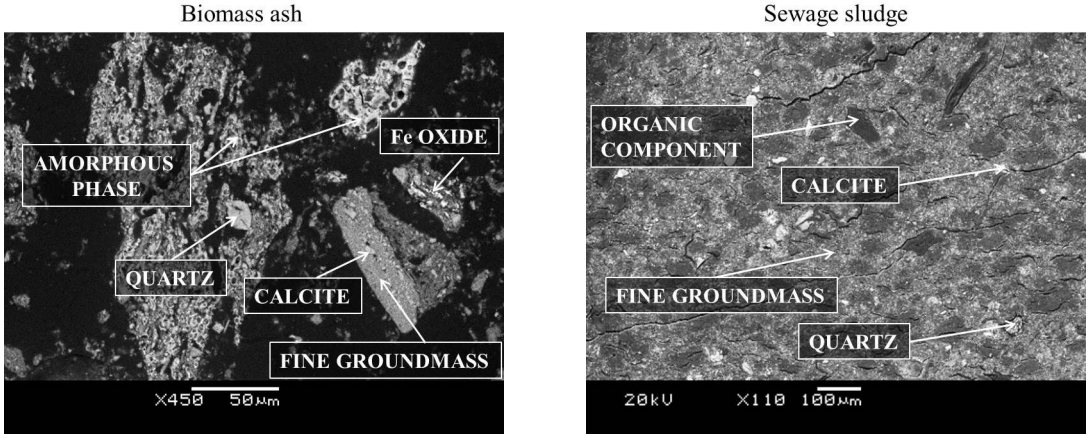

Figure 3. SEM micrographs of the sewage sludge and biomass ash investigated (phases identified on a basis of the combination of XRD and SEM/EDS).

The solid part of the sewage sludge consists of fine material (grains of various shapes, sized between 1 µm and 150 µm), with the larger grains embedded by a fine ground mass (Figure 3). EDS analysis identified larger carbonate grains (of calcite and dolomite) and quartz, as well as grains of organic phase. Calcite was identified and differentiated from portlandite and lime based on the EDS analysis results, which showed a Ca to O atomic percentage ratio of 1:3.

The biomass ash is also a fine material with an average grain size of approx. 90 µm. Larger grains of calcite, quartz, and portlandite, in addition to some iron oxides phases, are shown to be embedded in a fine groundmass (Figure 3). The amorphous phase of the sample consists of irregularly-shaped grains with a amorphous groundmass, in which small round pores can be observed. EDS analysis revealed that the amorphous phase primarily consisted of Si, Al and Ca in varying proportions (Figure 4), with smaller amounts of the elements K, Na, Mg, Cl and Fe. SEM/EDS further identified calcium sulphate and barium sulphide.

Results from QXRD analyses of the sewage sludge and biomass ash are shown in Table 3. Amorphous phase is the most abundant component of the sewage sludge, accounting for more than two thirds of its overall weight. The large amount of non-crystalline phase reflects the origin of the material, which contains a high proportion of organic material. Calcite (ICSD No. 73446) is the most abundant crystalline phase in sewage sludge, accounting for more than one quarter of its total. Additional, minor phases - dolomite (ICSD No. 66333) and quartz (ICSD No. 174) - are present in amounts of less than 2% by weight.

The two main components of biomass ash are amorphous phase and calcite (ICSD No. 73446), which, together, make up 75% of the ash by weight. Lime (ICSD No. 75786) and portlandite (ICSD No. 202220) are present in the amounts of 8.1 and 5.4 wt%, respectively, while talc (ICSD No. 26741), gehlenite (ICSD No. 158171) and quartz (ICSD No. 174) are present as minor phases. Since the ash is a residue from the high-temperature combustion of

biomass during the incineration process, it is partially in amorphous state and contains lime, which later, at least partially, hydrated and carbohydrated to portlandite and calcite. Namely, ashes rich in lime and portlandite are prone to hydration and carbonation when exposed to water. Under natural conditions or during curing in a climatic chamber, there is sufficient moisture and CO_2 available to convert both phases into calcite. It is well known that lime reacts quickly with moisture due to its highly hydrophilic nature. Similarly, portlandite is a well-known phase that reacts with CO_2 (27-29).

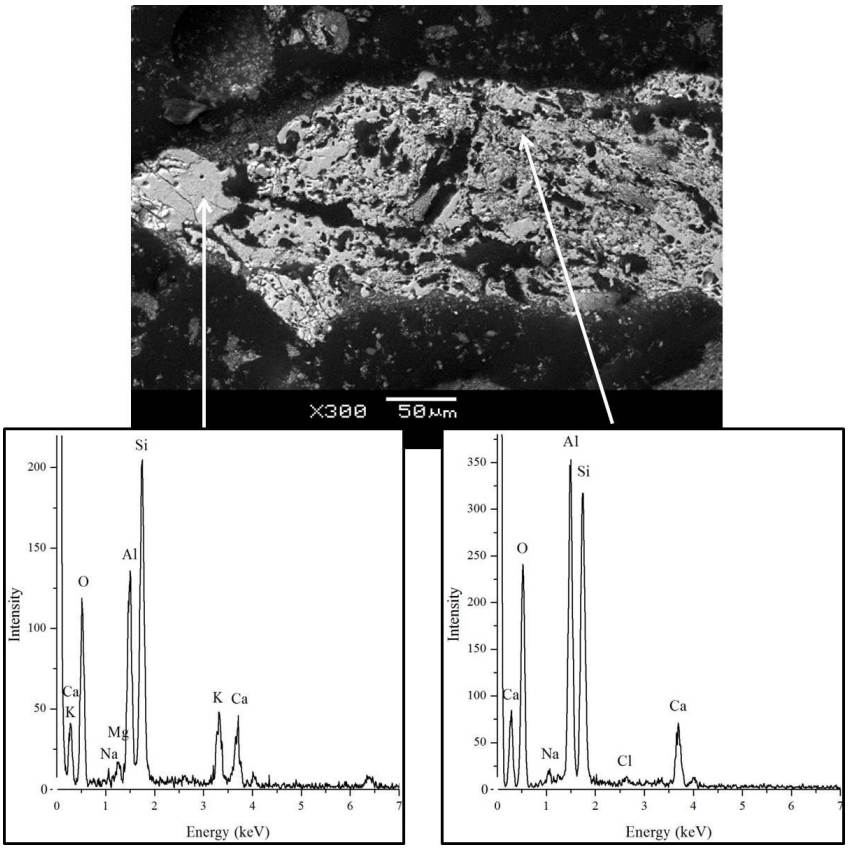

Figure 4. Results of the semiquantitative chemical analysis (EDS), showing an SEM micrograph detailing the amorphous phase in paper ash.

With the exception of gehlenite, which is considered to exhibit very low hydraulic activity and present in biomass ash in a low quantity (<4 wt.%), no other crystalline hydraulic phase was detected in either the ash or the sewage sludge.

Table 3. Results of the QXRD analysis with respect to the biomass ash and sewage sludge investigated including GOF values of the QXRD.

Phase composition (wt%)	Sewage sludge	Biomass ash
amorphous	70.4	36.6
calcite	27.0	38.8
dolomite	1.7	-
quartz	0.9	3.5
lime	-	8.1
portlandite	-	5.4
gehlenite	-	3.7
talc	-	3.9
GOF	1.44	1.69

The chemical compositions of the dried sewage sludge and biomass ash are presented in Table 4.

FTIR spectra of the sewage sludge and biomass ash are shown in Figure 5. The FTIR absorption bands at ~2515, 1796, 1428, 875 and 713 cm^{-1} confirm the presence of calcite in the sewage sludge. The band at ~1033 cm^{-1} confirms quartz. Absorption bands of the FTIR spectrum at ~1733 and ~1246 cm^{-1} indicate the presence of hemicelluloses (30). Furthermore, the aliphatic methylene absorption bands at 2956, 2923 and 2852 cm^{-1} and 1656 cm^{-1} (assigned to the C=O vibrations of amides, CO_2 vibrations of carboxylates and C=C vibrations of aromatics and alkenes, respectively) originate from the microbial biomass (30, 31).

The FTIR spectrum of the biomass ash confirms the presence of portlandite (shown by the absorption band at ~3644 cm^{-1}) and calcite (indicated by absorption bands at ~2515, 1797, 1428, 875 and 713 cm^{-1}). The bands at ~995 and 992 cm^{-1} represent Al–O vibrations and asymmetric stretching vibrations of Si–O–Si, respectively, indicating the presence of aluminosilicate phases.

Table 4. Chemical analysis of the dried sewage sludge and biomass ash

Chemical composition (wt%)	Sewage sludge	Biomass ash
SiO_2	3.07	11.37
Al_2O_3	1.51	8.26
Fe_2O_3	0.25	0.39
CaO	11.81	47.94
P_2O_5	1.64	0.17
MgO	0.88	1.70
K_2O	0.37	0.27
Na_2O	3.28	0.17
TiO_2	0.05	0.18
SO_3	1.58	0.31
Cl^-	0.074	0.001
LOI 950 °C	74.61	27.26

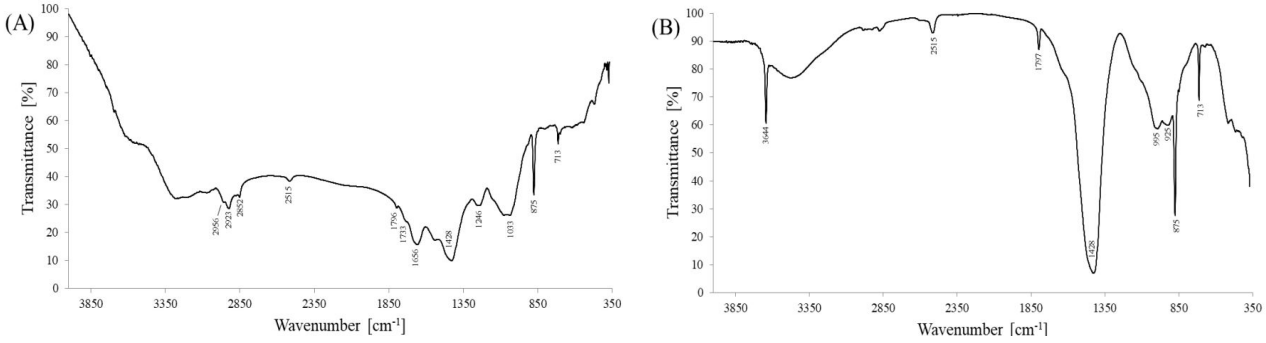

Figure 5. FTIR spectra of the sewage sludge (a) and biomass ash (b).

As shown in Table 4, there is a clear difference between the chemical compositions of the two raw materials. While LOI in the biomass ash was 27.26%, it was much higher in the sewage sludge (74.61%), mainly due to the presence of organic matter (TOC amounted up to 26,4 %, (32) and carbonates. In addition, the biomass ash is enriched with SiO_2, Al_2O_3 and Fe_2O_3 content associated with the amorphous phase and, to a lesser extent, with other phases such as gehlenite and talc. The CaO content, which is mainly related to the presence of calcite, lime and portlandite, is higher in the biomass ash. The alkali content is higher in the sewage sludge, with K_2O ranging from 0.37 % to 1.71 % and Na_2O from 0.87 % to 3.28 %. The SO_3 content of the raw materials studied ranged from 1.03% to 1.58%, and was also higher in the sewage sludge, while the TiO_2 content ranged from 0.05% to 1.08%. The MnO content varied between 0.04% and 0.17%. Sewage sludge was found to have an increased Cl^- content, although the values remained below the requirements of the EN 197-1 standard (0.10 %).

3.2. Characterization of the sludge-ash-composite

3.2.1. QXRD

The phase composition of the composite material prepared from the sludge and ash changed over time, due to progression of the hydration process. The QXRD results of the sludge-ash composite (Table 5) show calcite and calcium aluminate hydrates (C−A−H) as the main crystalline phases in all seven samples (3D-90D, KARB), while portlandite, talc, quartz and dolomite were identified as minor phases. Due to its hygroscopic properties, lime was only detected in the sample at 3 days (3D). Vaterite was detected in the carbonated sample (KARB), with the most pronounced peak occurring at 27.048 °2θ. The total amount of amorphous phase in the samples ranged between 49 and 38 wt%.

It is evident that progression of the hydration reaction in the sludge-ash composite is accompanied by the formation of hydration products (Table 5). Among the newly-formed hydration products in the sludge-ash composite, XRD analysis identified various different C-A-Hs − namely calcium hemicarboaluminate (Hc) (33), calcium monocarboaluminate (Mc) (ICSD No. 59327) and hydrocalumite (Hy) (ICSD No. 63251). Hc and Mc are the most abundant hydration products, with Hy only present in small amounts (less than 1 %).

Since the amorphous phase of the sewage sludge reflects the non-hydraulic organic matter (as confirmed by results of the LOI), and the content of the poorly hydraulic gehlenite in the paper ash is low, it can be concluded that the amorphous phase of the biomass ash represent the latent hydraulically-active component in the composite investigated. The amorphous phase of the biomass ash contributes alumina and (at least to a certain degree) calcium to the composite system in sufficient amounts for the formation of C−A−H phases in the sludge-ash composite. The lime and portlandite act as agitators (by increasing the pH of the porous solution) for dissolution of the amorphous ash phase of the composite. Figure 3 shows results of the QXRD analyses of the hydration products (Hc, Mc, Hy), portlandite, calcite and amorphous phase in the sludge-ash composite as a function of the hydration time. The amount of portlandite is small, and decreases over time (Figure 6). This observation can be attributed to the previously-mentioned fact that calcium hydroxide partially acts as an activator for hydration of the latent hydraulic component (34) and, to a certain extent, carbonatizes to calcite. Figure 6 also shows that hydration of the amorphous phase decreases over time. As already discussed, this decrease observed is attributed to the reactivity of the amorphous phase of the biomass ash and the subsequent formation of hydration products.

Table 5. Results from QXRD analysis of the sludge-ash composite at various time intervals including GOF values of the QXRD.

Phase composition (wt%)	3 D	7 D	14 D	28 D	56 D	90 D	KARB
amorphous	49.1	48.9	47.3	46.4	44.9	44.9	38.5
calcite	35.7	36.1	35.2	34.4	33.1	35.1	47.1
dolomite	0.0	0.0	0.0	0.0	1.5	0.0	0.0
hemicarboaluminate	10.2	10.9	7.7	7.0	6.9	6.2	3.6
hydrocalumite	0.6	0.7	0.6	0.6	0.5	0.4	0.3
lime	2.0	0.0	0.0	0.0	0.0	0.0	0.0
monocarboaluminate	0.8	2.1	7.5	10.7	11.7	12.6	7.8
portlandite	1.4	1.1	0.9	0.6	0.6	0.3	0.0
quartz	0.1	0.1	0.4	0.2	0.8	0.5	1.5
talc	0.1	0.1	0.4	0.1	0.0	0.0	0.0
vaterite	0.0	0.0	0.0	0.0	0.0	0.0	1.2
GOF	1.43	1.41	1.39	1.35	1.36	1.35	1.42

Conversely, a clear transition of Hc to Mc can be observed as hydration time increases (Figure 6).

Hc is formed immediately after 3 days of hydration and its amount remains more or less constant (10 wt%) during the first 7 days. After this period, the amount of Hc begins to gradually decrease. In contrast, after 3 days Mc is only present in very small quantities (< 1 wt%). The amount of Mc steadily increases in line with the hydration time. Mc develops most strongly during the first 14 days of hydration (increasing from 0.8 to 7.4 wt.%). After this period, up until 90 days, the amount then increases far more slowly. Similar to as in Portland cements, which contain calcite (35), Hc formed at the beginning of hydration and then gradually converted to Mc as the hydration progressed. The mechanism of carboaluminate conversion is consistent with the literature data: at 25 °C, Hc is not stable in the presence of excess

calcite (36), and monocarboaluminate is the energetically-preferred carboaluminate phase (37). The tendency for the formation of Hy is similar to that of Hc and could also be correlated with Mc, but since the total amount of this phase is very small (<1wt.%), no further conclusions can be drawn.

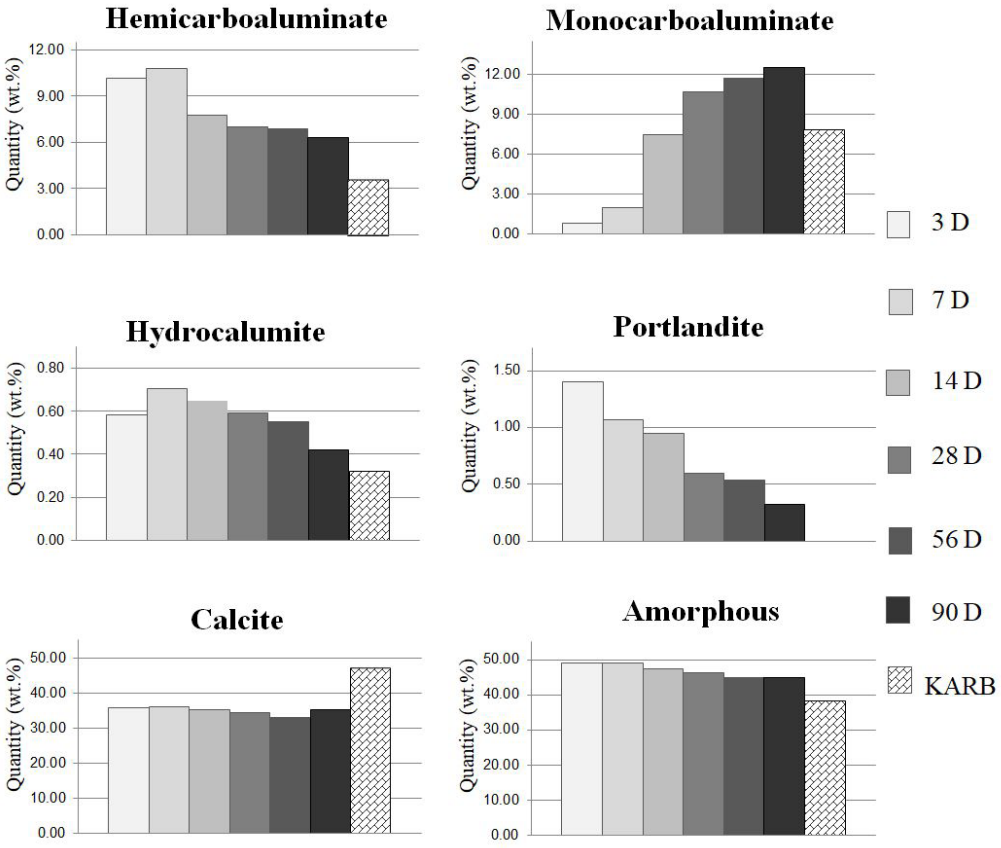

Figure 6. Results from QXRD analysis of the sludge-ash composite with respect to the hydration products, portlandite, calcite and amorphous phase.

The total amount of crystalline hydration products, as determined by QXRD - namely both the carboaluminate phases, which represent the vast majority, and the overall sum of all the C-A-H's (carboaluminates with hydrocalumite) - is highest after 28 days of hydration. As the duration of hydration increases, the total amount remains more or less constant until the 90th day of hydration (varying by only 1 %).

A marked decrease was observed in the carboaluminate phases of the carbonated sludge-ash composite (KARB), with an obvious increase in calcite and the formation of vaterite (Figure 6, Table 3). Various studies of hydraulically active systems have shown that, in addition to CH and C−S−H, C−A−Hs are also susceptible to carbonation (38). This observation can be attributed to a decrease in the carbonate aluminate phases of the carbonated sludge-ash composite (KARB). Since carbonation of all the calcium-containing phases significantly contributes to the formation of $CaCO_3$ (39), the calcite content in the KARB sample is higher than that of the other samples studied, being slightly more than 10 wt%. It has been reported that vaterite and aragonite form as the primary carbonation products of cementitious systems (40). The partial precipitation of $CaCO_3$ as vaterite in the KARB sample indicates a predominance of the kinetic factor during carbonation of the sludge-ash composite (41). Over time, the vaterite polymorph of $CaCO_3$ transforms into the more stable polymorph, calcite (39).

3.2.2. FTIR spectroscopy

The formation of new hydration products is also evidenced by the FTIR spectra (Figure 2, Table 6). This is particularly evident by the appearance of additional bands at ~ 3675 (I), 3640 (II), 3621 (III), 3541 (VI) and 3523 (V) cm^{-1}, which correspond to OH stretching vibrations in the newly formed carboaluminates, i.e. Hc and Mc phases (42).

Table 6. Bands identified in FTIR spectra of the sewage sludge-biomass ash composite at different hydration periods (cm^{-1}).

	3 D	7 D	14 D	28 D	56 D	90 D	KARB
I	3674	3675	3675	3675	3675	3675	3675
II	3643	3643	3644	3643	3641	3641	3641
III	3622	3623	3623	3624	3623	3623	3622
IV		3541	3541	3541	3541	3541	3541
V		3526	3526	3525	3525	3526	3524
VI	3464						
VII			3355	3358	3356	3354	3353
VIII	2985	2987	2984	2986	2986	2984	2986
IX	2876	2878	2868	2876	2877	2871	2877
X	2514	2515	2514	2512	2513	2514	2514
XI	1797	1797	1798	1797	1797	1798	1797
XII		1637	1644	1640	1639	1642	1630
XIII	1621						
XIV	1428	1425	1426	1423	1424	1424	1422
XV	1170	1172	1173	1173	1172	1172	
XVI	1009	1008	1009	1008	1007	1006	1005
XVII	953	953	956	956	957	959	964
XVIII	875	875	875	875	875	875	875
XIX	848	848	848	848	848	848	848
XX	792	795	796	794	792	794	793
XXI	713	713	713	713	713	713	713
XXII	671	666	669	669	671	669	667
XXIII	586	584	583	579	579	584	584
XXIV	530	531	535	535	536	536	538
XXV	466	466	465	466	464	465	465
XXVI				454	452	452	450
XXVII	423	423	423	423	423	423	424
XXVIII	394	391	390	395	392	394	
XXIX		383	380	385	381	380	
XXX		375	374	378	375		

As can be seen in Figure 4, the band height and areas of the band at ~3675 (I) cm^{-1} increase with curing time, indicating the progressive formation of Mc phase. A strong increase can be observed during the first 14 days, after which time the proportion slowly increases. In the carbonated sample, however, the amount significantly decreases. On the other hand, the band at ~3640 cm^{-1}, characteristic of portlandite (in smaller extent is also contributed Hc), shows an exponential decrease in line with curing time, as evidenced by a decrease in the band heights and areas (Figure 7). A pronounced consumption of portlandite is observed during the first 14 days, after which time the consumption rate slowed and was no longer observed in the carbonated sample. Besides, as hydration process progress, Hc gradually converts to Mc (35). This is consistent with the results obtained from the XRD analysis.

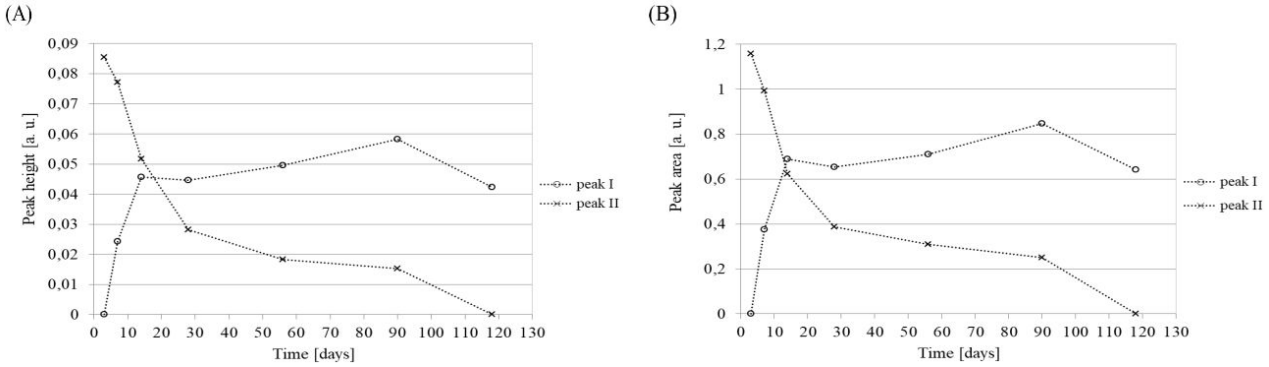

Figure 7. Average height (a) and average area (b) for selected FTIR absorption bands assigned to Mc (~3675 cm^{-1} –band I) and portlandite and/or Hc (3643 cm^{-1}–band II).

The band at ~1009 (XVI) cm^{-1} was assigned to the asymmetric Si−O stretching vibrations of the C−S−H phase. As can be seen from the band heights and areas in Figure 5, the C−S−H phase does not change much over time. Moreover, the band heights and areas of band at ~950 (XVII) cm^{-1}, assigned to the Al-O vibrations of carboaluminates (as well as, to a certain extent, the Si−O vibrations in C−S−H; (42), increased with hydration time. In the carbonated sample, the band heights and areas both decreased for both bands, indicating lower C−S−H and carboaluminate contents (Figure 8).

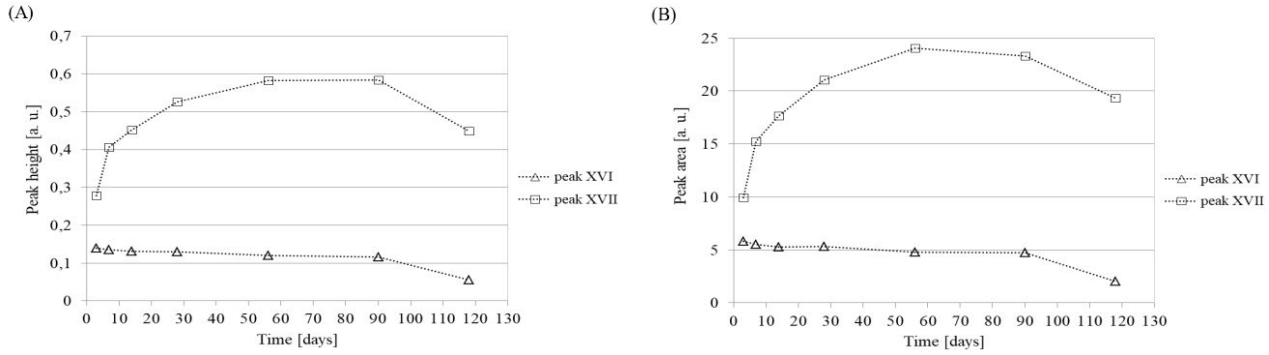

Figure 8. Average height (a) and average area (b) for selected FTIR absorption bands assigned to C–S–H (~1009 cm^{-1} – band XVI) and carboaluminates (~953 cm^{-1} – band XVII).

As can be seen in Figure 9, the XVI band shifts slightly to a lower wavenumber as hydration time increases, indicating the incorporation of a heavier ion into the crystal structure i.e. Al uptake is reflected in the formation of C−(A)−S−H (43). Conversely, the XVII band shifts to higher wavenumbers which was attributed to the polymerization of silica during the ageing and decalcification process (42), as the Si ion is lighter than the Ca ion, resulting in higher vibrational frequencies.

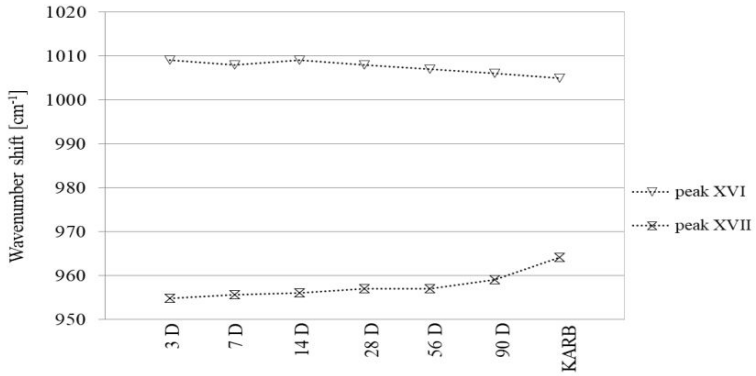

Figure 9. Wavenumber shift for the Si-O band (band XVI attributed to C–S–H) and the Al-O band (band XVII attributed to carboaluminates).

With respect to the band heights and area ratios, the decreasing ratio of the XVI/XVII bands indicates that the Mc phase increased exponentially over time (Figure 10).

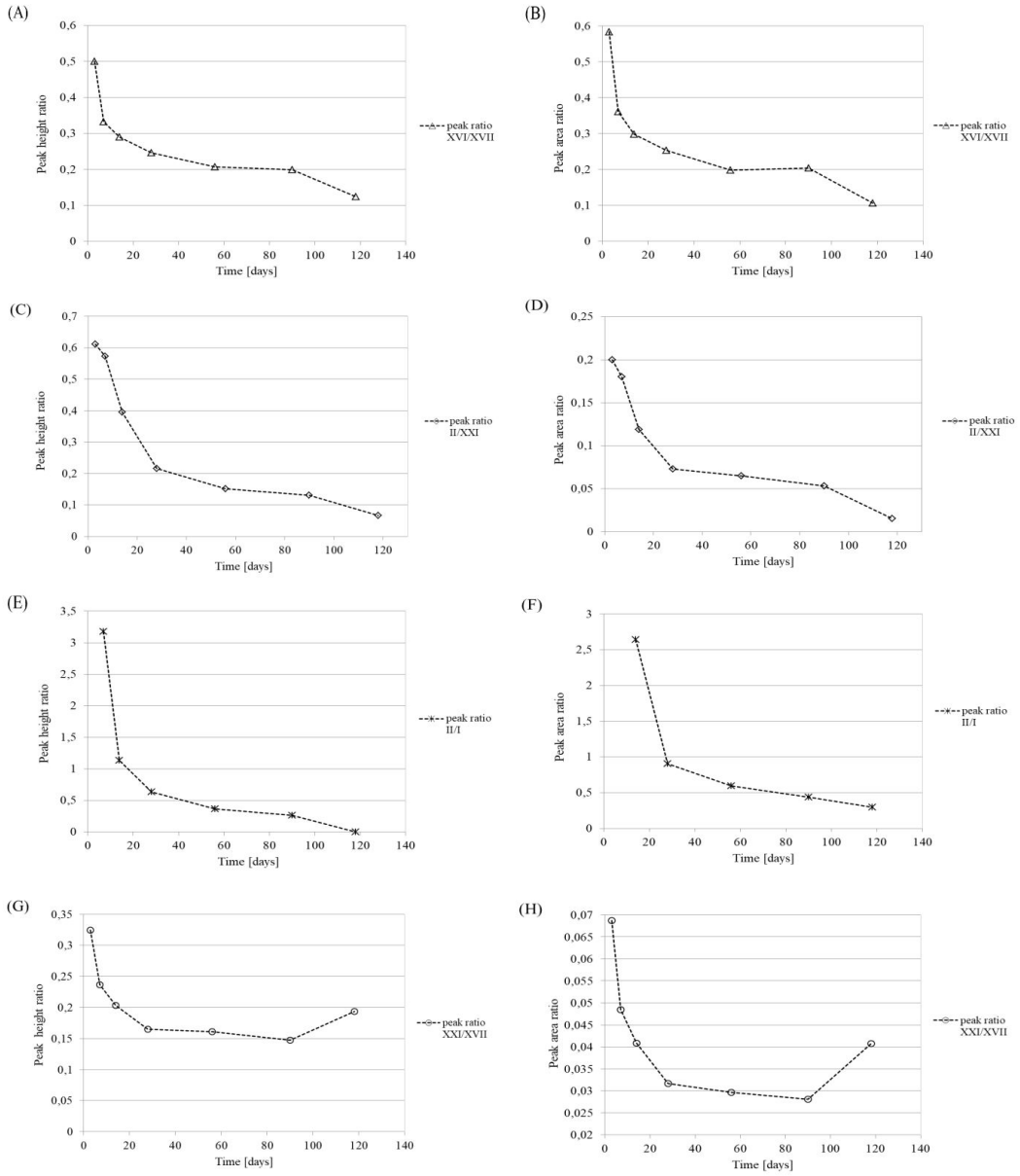

Figure 10. Band height and band ratio for selected FTIR absorption bands (a-b) C–S–H/carboaluminates ratio – band ratio XVI/XVII (c-d) portlandite/calcite ratio – band ratio II/XXI, (e-f) portlandite/Mc ratio – band ratio II/I, and (g-h) calcite/ carboaluminates ratio - XXI/XVII.

In carbonated sample the ratio is even lower indicating higher Mc phase content. In addition, the decreasing ratio of II/XIV bands indicates a decrease in the amount of portlandite, alongside a concurrent increase in the amount of calcite. The same applies to the ratio of the II/I bands, indicating an increase in the amount of the Mc phase and a decrease in the amount of portlandite and Hc over time. The band ratio XXI/XVII decreases over time, indicating the formation of new hydration products as the hydration progresses. In the carbonated sample, however, this ratio increased indicating higher calcite content.

3.2.3. SEM/EDS

SEM/EDS analysis confirmed the (latent) hydraulic activity of the biomass ash, as shown by enlargement of the reaction rims around the biomass ash relics as the duration of hydration increased, which can be seen in Figure 11. After 3 days of hydration, smaller reaction edges can be observed around the individual ash grains, but at this stage not

all grains have started to hydrate. As the duration of hydration increases, larger reaction rims and smaller biomass ash residues were observed, due to the formation of larger amounts of hydration products. After 28 days, the dimensions of the hydration rims grew to a lesser extent than previously. In the 90-day-old sample, the boundaries between the reaction edges and the ash residues are often difficult to define due to the progression of hydration. Firm contact exists between the individual grains of biomass and sludge in the matrix/groundmass of the sludge-ash composite.

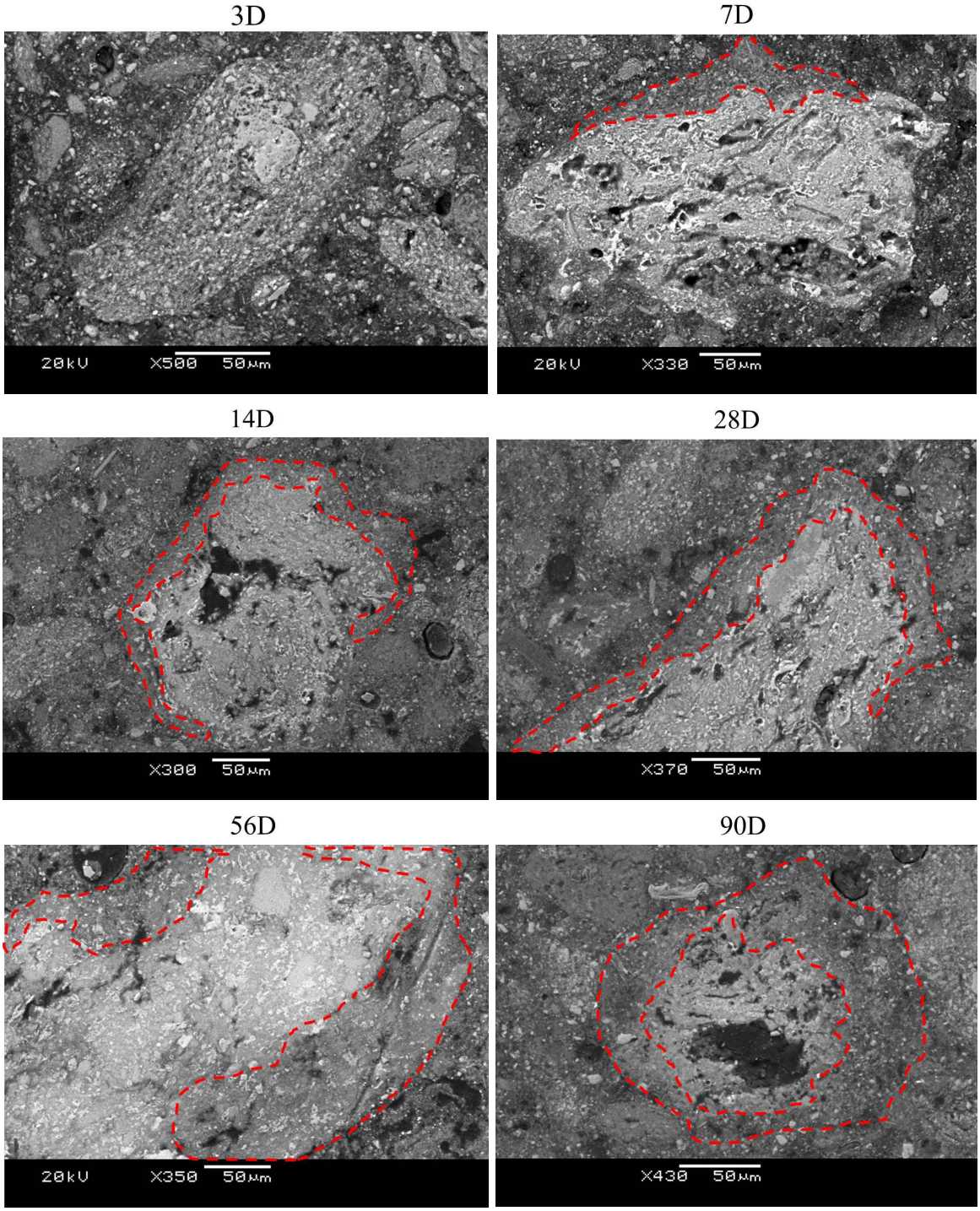

Figure 11. SEM micrographs of the sludge-ash composite at various times of hydration (3, 7, 28, 56 and 90 days). The reaction rims of the biomass ash grains are indicated by the dashed red line.

Figure 12 shows the results of the SEM/EDS analysis of the various hydration products.

Whilst the XRD analysis defined only the C−A−H phases, other phases are clearly present in the sludge-ash composite. Some weakly crystalline hydration products with a net/foil-like to fibrillar morphology were also identified, consisting of a combination of Ca and Si or Ca, Si and Al. It can be concluded that some C−S−H and C−A−S−H phases mixed with each other or C−A−H were also formed during hydration of the composite investigated, as also indicated by FTIR analysis (44).

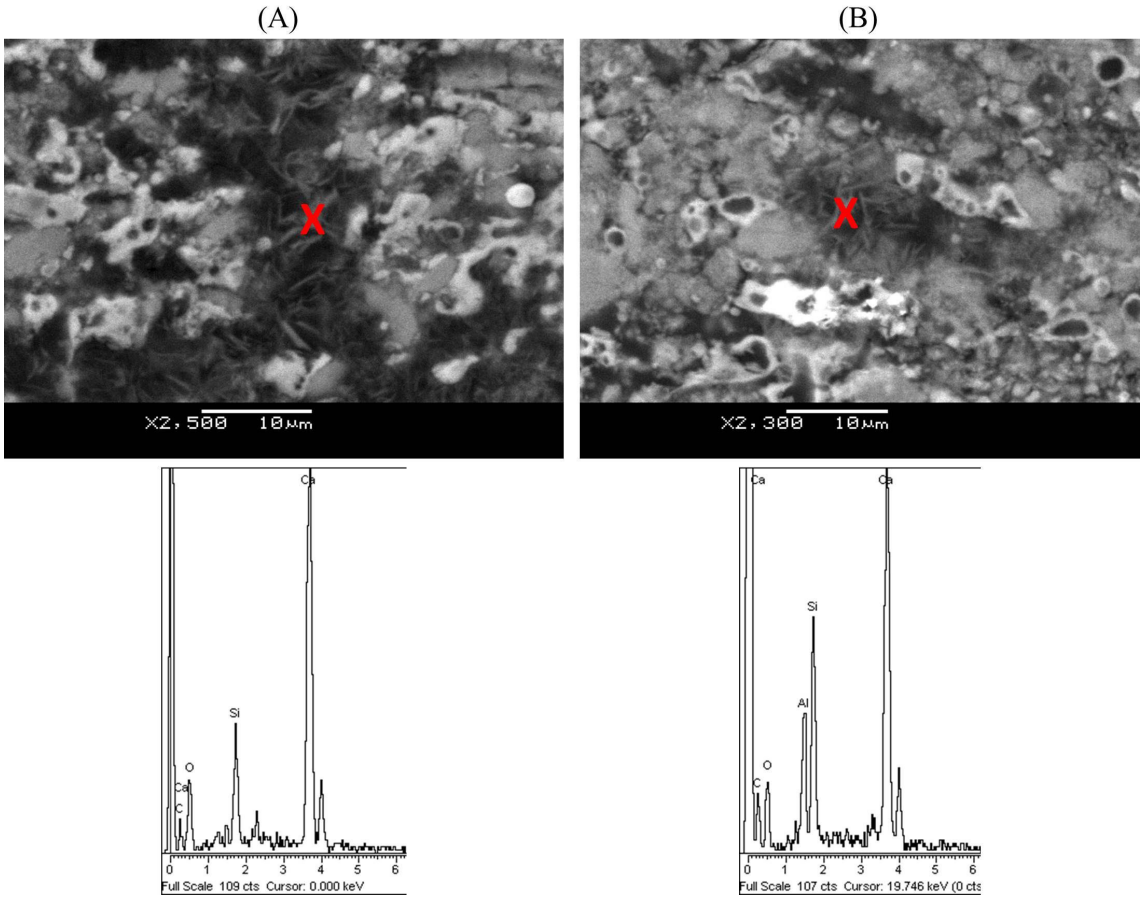

FIGURE 12. SEM micrographs of the various hydration products formed in the 90 D composite, with results of the EDS analysis (point analysis designated with red "x") for the C– S–H (A) and C–A–S–H phases (B).

3.2.4. Physical properties

The pore size distribution of the sludge-ash composite at various times of hydration is shown in Figure 13.

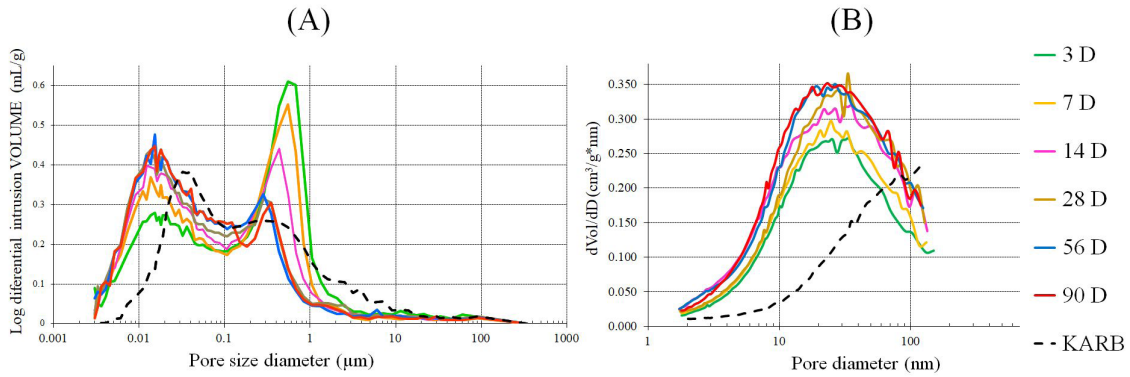

FIGURE 13. Pore size distribution of the sludge-ash composite at various times of hydration, as measured by MIP (A) and nitrogen gas sorption (B).

The MIP results (Figure 13. A) show a clear bimodal pore distribution in all the samples tested, with one peak present in the large capillary region (10- 0.05 μm), centred at approximately 0.29 - 0.69 μm, and a second in the region of medium capillaries with gel pores (< 0.05 μm) (45), centred at approximately 0.016 μm. In the early stages of hydration (up to 28 days), the number and, to a lesser extent, size of the large capillaries decreased as the hydration time increased. In contrast, the number of medium capillaries and gel pores increased during this period, as also confirmed by the nitrogen gas sorption analysis (Figure 13.B). Later on in the process (after 28 days), the changes in pore size distribution are clearly much slower than during the early stages, suggesting that the main features of the internal microstructure generally remained unchanged until the 28th day of hydration.

The formation of hydration products over time is in good agreement with the increasing proportion of pores smaller than 50 nm in diameter (as shown in Figure 13 A and B), which are usually classified as gel and capillary pores of the C−(A)−S−H structure (45, 46). The changes in the peak in the area of the large capillaries and the peak in the area of the smaller pores reflect the fact that larger pores gradually close due to the newly-formed hydration products.

A clear microstructural refinement of the carbonated sewage sludge-ash composite sample (KARB) can also be seen in Figure 13. The pore size distribution of the KARB sample shows a less pronounced bimodal distribution, including one broad peak with a smaller shoulder and one larger peak, located at 0.45 and 0.038 μm, respectively (Figure 13. A). The main peak, representing the large capillaries, decreased in the KARB sample, while the peak in the middle capillary region with gel pores increased from 0.017 μm to 0.037 μm. The carbonation of hydration products to calcite is accompanied by a reduction in the number of pores larger than 0.1 μm (47). For pores smaller than approximately 0.03 μm, the difference in pore volume between the carbonated and non- carbonated samples increased as the pore size decreased. This effect can be attributed to the carbonation of hydrated calcium (aluminium) silicates (C−(A)−S−H) in the composite, which decreases the amount of the C−(A)−S−H gel phase and reduces the pore volume in the region of approximately < 0.05 μm, which is associated with gel and capillary pores of the C−S−H structure (45, 46, 48). A global reduction in the volume of pores with a diameter between 0.010 and 0.1 μm as a result of the effects of carbonation has also been reported for mixed cementitious composite material systems (49).

The porosity, total pore area, mean and median pore diameters of the sludge-ash composite samples investigated are shown in Figure14.

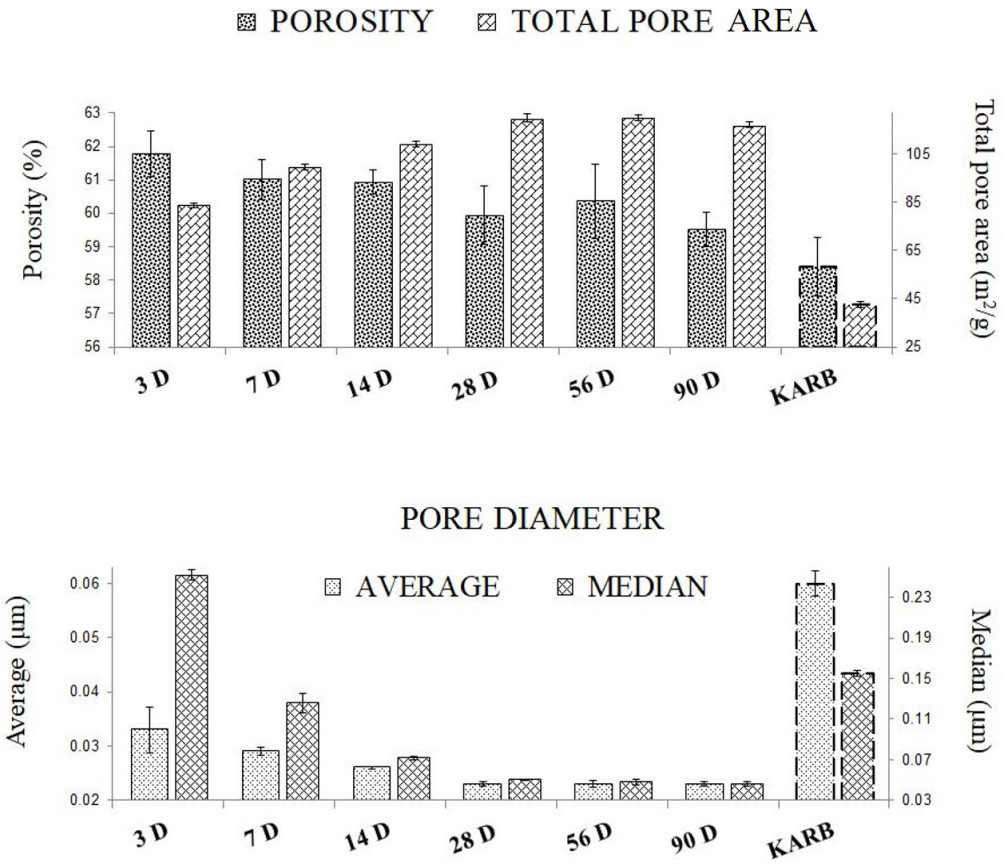

Figure 14. Porosity, total pore area, average and median pore diameters of the sludge-ash-composite at different times of hydration and following carbonation. Average values ± standard deviation (represented by bars) were calculated for each measurement.

The porosity (%) shows a general downward trend as the hydration time increases. The lowest porosity is observed in the carbonated sample. In contrast, the total pore area increases, although after 28 days of hydration it changes only slightly as curing times are extended. The lowest total pore area is observed in the carbonated sample.

The total porosity decreases as hydration time increases, as the number of large capillaries decreases, whilst the number of pores sized below 0.05 μm (medium capillaries with gel pores) increases. At the same time, the total pore area increases, due to the formation of a greater number of smaller pores as hydration progresses. The refinement of pore size after carbonation means the carbonated sample has the lowest porosity overall. Compaction with reduced porosity due to carbonation has also been observed in cement composites (48, 50). Due to the significant shift of pores sized < 0.05 μm (mean capillaries with gel pores) to larger pores, the total pore area is smallest in the carbonated sample (KARB). These findings are corroborated by the smaller pore diameters (Figure 14) observed following longer hydration times, and by the fact that the average and mean pore size were highest in the carbonated sample. Consistent with results from the FTIR and XRD analyses, the largest decrease in total pore diameters is observed by day 28, indicating that the main hydration products are formed during the first 14 days.

The specific BET surface areas of the sewage sludge-ash composite samples investigated are shown in Figure 15. The specific BET surface areas are consistent with results from the MIP analysis, as a higher SSA correlates with the increase in number of smaller pores associated with the formation of hydration products over time.

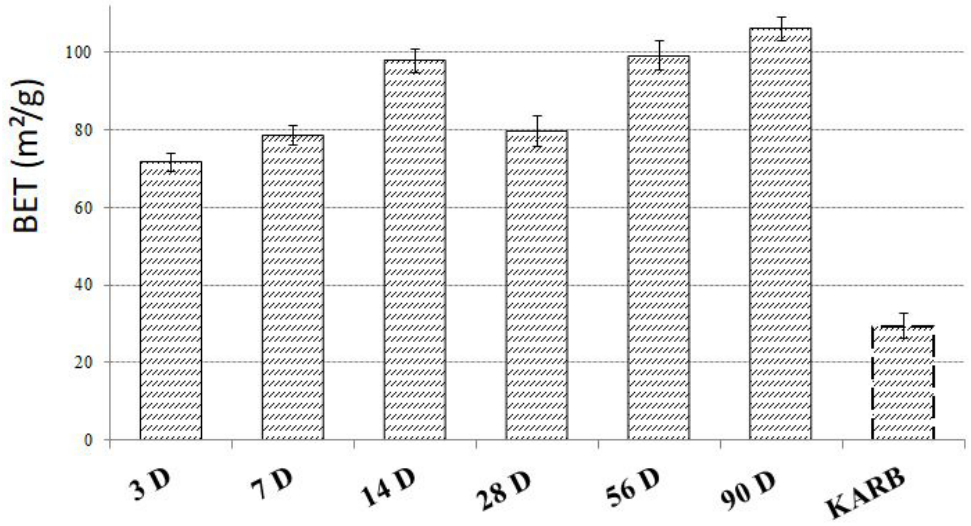

Figure 15. BET specific surface areas of the sludge-ash composite at investigated times of hydration and after the carbonation. Average values ± standard deviation (represented by bars) calculated for each measurement.

The specific BET surface area increased gradually as the duration of hydration increased. Sample 90D exhibited the highest BET specific surface area, confirming once again that larger amounts of mean capillary and gel pores were formed when the hydration time was longer, which can be attributed to the higher degree of hydration of the composite tested. In contrast, the lowest BET values were observed in the carbonated sample, which can be attributed to the smaller amounts of small capillary and gel pores in this sample, resulting from pore size redistribution during carbonation.

Results from the detailed microstructural characterization presented in this study are in good agreement with the mechanical properties (compressive strength) of the sludge-ash composite reported by Pavšič et al. (19), which showed an increase in compressive strength in line with increasing curing times. This was attributed to the formation of new mineral phases in the composite over time and the resulting redistribution of the microstructure.

4. CONCLUSIONS

By adapting waste materials, in terms of the composition and properties of the material, to the availability and needs of the construction industry, high-volume residues that currently have little or no end use can be utilized, thus putting industrial symbiosis into practice. It is crucial to understand the mechanisms of phase and porosity evolution in construction composites, as the microstructure of a material directly determines its mechanical-physical properties. In this study, the microstructural evolution of a sewage sludge/ biomass ash composite was investigated by determining the phase composition and porosity parameters over time. The conclusions of the study are as follows:

1. The composition of biomass ash makes it possible to provoke a hydration reaction, mainly due to the presence of lime, portlandite and amorphous phase components. Upon contact with moisture from the sewage sludge, cementitious hydration products are formed.

2. As the duration of hydration increases, the portlandite and amorphous phase are consumed, resulting in the formation of C−A−H and C−(A)–S−H, which mix in the composite's newly-formed matrix. As the system is rich in calcite, monocarboaluminate is favoured over hemicarboaluminate.

3. The majority of the hydration process is completed during the first 28 days of hydration. After a period of 28 days, the reaction rate slows down.

4. As the hydration period increases, the number (and size) of large capillaries significantly decreases, because newly-formed hydration products fill free space between the grains, forming a matrix within the composite.

5. Conversely, the amount of medium-sized capillaries and gel pores increases during the same period, as these pores are assigned to the C−(A)−S−H structure as gel and capillary pores.

6. The primary features of the internal structure are generally formed within the first 28 days of hydration, after which time changes occur far more slowly.

7. The results confirm that the composite material investigated shows promising potential for CO_2 sequestration. Further research should include systematic analysis of the carbonation process in the building composite from sewage sludge and biomass ash investigated.

Acknowledgements

Petra Šajna is acknowledged for her help with FTIR.

Funding Sources

This work was financially supported by the ARIS Programme Group P2-0273, ARIS Infrastructure group I0-0032 and projects ARRS J1-4413, ARRS L7-3185. The Metrology Institute of the Republic of Slovenia is acknowledged for use of their XRF equipment.

Authorship contribution statement

Vesna Zalar Serjun: Data curation, Formal analysis, Investigation, Methodology, Validation, Visualization, Writing - original draft, Writing - review & editing.

Sabina Dolenec: Conceptualization, Investigation, Methodology, Writing - original draft, Writing - review & editing

Matej Dolenec: Formal analysis, Investigation, Methodology, Writing - review & editing.

Ana Mladenović: Conceptualization, Data curation, Funding acquisition, Methodology, Supervision, Validation, Visualization, Writing - review & editing.

Primož Pavšič: Conceptualization, Data curation, Investigation, Methodology, Supervision, Writing - original draft, Writing - review & editing.

Declaration of competing interest

The authors of this article declare that they have no financial, professional or personal conflicts of in-terest that could have inappropriately influenced this work.

REFERENCES

1. Kiselev A, Magaril E, Magaril R, Panepinto D, Ravina M, Zanetti MC. 2019. Towards circular economy: evaluation of sewage sludge biogas solutions. Res. 8(2):91. https://doi.org/10.3390/resources8020091.
2. Bianchini A, Bonfiglioli L, Pellegrini M, Saccani C. 2016. Sewage sludge management in Europe: A critical analysis of data quality. Int. J. Environ. Waste Manag. 18(3):226-238. https://doi.org/10.1504/IJEWM.2016.080795.
3. Campo G, Cerutti A, Lastella C, Leo A, Panepinto D, Zanetti M, Ruffino B. 2021. Production and destination of sewage sludge in the piemonte region (italy): the results of a survey for a future sustainable management. Int. J. Environ. Res. Public Health. 18(7):3556. https://doi.org/10.3390/ijerph18073556.
4. Kalderis D, Aivalioti M, Gidarakos E. 2010. Options for sustainable sewage sludge management in small wastewater treatment plants on islands: The case of Crete. Desalination. 260(1-3):211–217. https://doi.org/10.1016/j.desal.2010.04.030.

5. Mislej V, Grilc V, Novosel B, Mladenovič A, Zalar Serjun V. 2022. Sewage sludge management at the central wastewater treatment plant Ljubljana: characterization of its properties, possibilities for sustainable utilization and legislative obstacles. Holist. Approach Environ. 12(1):9-25. https://doi.org/10.33765/thate.12.1.2.
6. Hudcova H, Vymazal J, Rozkošny M. 2019. Present restrictions of sewage sludge application in agriculture within the European Union. Soil Water Res. 14(2):104–120. https://doi.org/10.17221/36/2018-SWR.
7. Eurostat, Water statistics 2022.
8. Balkrishna A, Singh SK, Pathak R, Arya V. 2022. Sludge management: current scenario, available solutions and way forward. Authorea Preprints. https://doi.org/10.22541/au.164899217.73875491/v2.
9. Chang Z, Long G, Zhou JL, Ma C. 2020. Valorization of sewage sludge in the fabrication of construction and building materials: A review. Resour. Conserv. Recycl. 154:104606. https://doi.org/10.1016/j.resconrec.2019.104606.
10. Monte MC, Fuente E, Blanco A, Negro C. 2009. Waste management from pulp and paper production in the European Union. Waste Manage. 29(1):293−308. https://doi.org/10.1016/j.wasman.2008.02.002.
11. Zhang Z, Macquarrie DJ, Aguiar PM, Clark JH, Matharu AS. 2015. Simultaneous recovery of organic and inorganic content of paper deinking residue through low-temperature microwave-assisted pyrolysis. Environ. Sci. Technol. 49(4):2398–2404. https://doi.org/10.1021/es505249w.
12. Di Fraia S, Uddin MR. 2022. Energy recovery from waste paper and deinking sludge to support the demand of the paper industry: a numerical analysis. Sustain. 14(8):4669. https://doi.org/10.3390/su14084669.
13. Steffen F, Janzon R, Wenig F, Saake B. 2017. Valorization of waste streams from deinked pulp mills through anaerobic digestion of deinking sludge. BioResour. 12(3):4547- 4566. https://doi.org/10.15376/biores.12.3.4547-4566.
14. Fifer Bizjak K, Likar B, Mladenovič A, Zalar Serjun V. 2021. Valorized deinking paper residue as fill material for geotechnical structures. Sci. Rep. 11:22363. https://doi.org/10.1038/s41598-021-01949-1.
15. European Commision. 2015. Best Available Techniques (BAT) Reference document for the production of pulp, paper and board. Industrial Emissions Directive 2010/75/EU (Integrated Pollution Prevention and Control). Retrieved from https://publications.jrc.ec.europa.eu/repository/handle/JRC95678 (acessed 22 August 2023).
16. Bajpai P. 2015. Generation of waste in pulp and paper mills. In: Management of Pulp and Paper Mill Waste. Springer, Cham. https://doi.org/10.1007/978-3-319-11788-1_2.
17. Martínez-Lage I, Velay-Lizancos M, Vázquez-Burgo P, Rivas-Fernández M, Vázquez-Herrero C, Ramírez-Rodríguez A, Martín-Cano M. 2016. Concretes and mortars with waste paper industry: Biomass ash and dregs. J. Environ. Manag. 181:863-873. https://doi.org/10.1016/j.jenvman.2016.06.052.
18. Mladenovič A, Hamler S, Zupančič N. 2017. Environmental characterisation of sewage sludge/paper ash-based composites in relation to their possible use in civil engineering. Environ. Sci. Pollut. Res. 24:1030–1041. https://doi.org/10.1007/s11356-016-7843-2.
19. Pavšič P, Mladenovič A, Mauko A, Kramar S, Dolenec M, Vončina E, Pavšič Vrtač K, Bukovec P. 2014. Sewage sludge/biomass ash based products for sustainable construction. J. Clean. Prod. 67:117-124. https://doi.org/10.1016/j.jclepro.2013.12.034.
20. European Commission. 2019. Communication from the Commission to the European Parliament, the Council, the European Economic and Social Committee and the Committee of the Regions, The Environmental Implementation Review 2019: A Europe that protects its citizens and enhances their quality of life. COM(2019) 149 final. Brussels. Retrieved from https://eur-lex.europa.eu/resource.html?uri=cellar:fcfafdcd-0abf-11ea-8c1f-01aa75ed71a1.0013.02/DOC_1&format=PDF, (acessed 22 August 2023).
21. Rao Meda S, Kumar Sharma S, Tyagi GD. 2021. Utilization of waste sludge as a construction material - a review. Mater. Today. Proc. 46(9):4195–4202. https://doi.org/10.1016/j.matpr.2021.02.762.
22. Swierczek L, Cieslik BM, Konieczka P. 2018. The potential of raw sewage sludge in construction industry - A review. J. Clean. Prod. 200:342-356. https://doi.org/10.1016/j.jclepro.2018.07.188.
23. Mymrin V, de Andrade C, Alekseev K, Avanci MA, Catai RE, Rolim R, Kiltzke W, da Silva DA, Ferraz FA. 2019. Structure formation processes of sustainable construction material from hazardous sewage sludge with additions of wood ash, and lime production waste. Int. J. Adv. Manuf. Technol. 105:5191–5201. https://doi.org/10.1007/s00170-019-04408-4.
24. Chakraborty S, Wan Jo B, Ho Jo J, Baloch Z. 2017. Effectiveness of sewage sludge ash combined with waste pozzolanic minerals in developing sustainable construction material: An alternative approach for waste management. J. Clean. Prod. 153:253-263. http://doi.org/10.1016/j.jclepro.2017.03.059.
25. Cline JP, Von Dreele RB, Winburn R, Stephens PW, Filliben JJ. 2011. Addressing the amorphous content issue in quantitative phase analysis: the certification of NIST standard reference material 676a. Acta Cryst. A67(4):357-367. https://doi.org/10.1107/S0108767311014565.
26. Zhang J, Scherer GW. 2011. Comparison of methods for arresting hydration of cement. Cem. Concr. Res. 41(10):1024–1036. https://doi.org/10.1016/j.cemconres.2011.06.003.
27. Bouzar B, Mamindy-Pajany Y. 2022. Manufacture and characterization of carbonated lightweight aggregates from waste paper fly ash. Powder Technol. 406:117583. https://doi.org/10.1016/j.powtec.2022.117583.
28. Bouzar B, Mamindy-Pajany Y, Mkahal Z, Benzerzour M. 2024. Pilot-scale natural carbonation of waste paper fly ash for stabilization of Ba and Pb. Green Technol. Sustainability 2:100075. https://doi.org/10.1016/j.grets.2024.100075.
29. Ottosen LM, Sigvardsen NM. 2024. Heavy metal leaching from wood ash before and after hydration and carbonation. Environ. Sci. Pollut. Res. https://doi.org/10.1007/s11356-024-33221-0.

30. Smidt E, Böhm K, Schwanninger M. 2011. The application of FT-IR spectroscopy in waste management, in: Nikolic G (Ed.), Fourier Transforms e New Analytical Approaches and FTIR Strategies. InTech. ISBN 978-953-307-232-6.
31. Smidt E, Meissl K, Tintner J. 2007. Investigation of 15-year-old municipal solid waste deposit profiles by means of FTIR spectroscopy and thermal analysis. J. Environ. Monit. 9:1378-1393.
32. Zavod za zdravstveno varstvo Novo Mesto, Report – Poročilo o preskušanju, Lab. št. 2012/3264, 2012.
33. Runčevski T, Dinnebier RE, Magdysyuk OV, Pöllmann H. 2012. Crystal structures of calcium hemicarboaluminate and carbonated calcium hemicarboaluminate from synchrotron powder diffraction data. Acta Crystallogr. B Struct. Sci. Cryst. Eng. Mater. B68:493-500. https://doi.org/10.1107/S010876811203042X.
34. Snellings R, Mertens G, Elsen J. 2012. Supplementary cementitious materials. Rev. Mineral. Geochem. 74(1):211-278. https://doi.org/10.2138/rmg.2012.74.6.
35. Ipavec A, Gabrovšek R, Vuk T, Kavčič V, Maček J. 2011. Meden A., Carboaluminate phases formation during the hydration of calcite-containing portland cement. J. Am. Ceram. Soc. 94(4):1238-1242. https://doi.org/10.1111/j.1551-2916.2010.04201.x.
36. Matschei T, Lothenbach B, Glasser FP. 2007. The AFm phase in Portland cement, Cem. Concr. Res. 37(2):118-130. https://doi.org/10.1016/j.cemconres.2006.10.010.
37. Matschei T, Lothenbach B, Glasser FP. 2007. Thermodynamic properties of Portland cement hydrates in the system CaO-Al_2O_3-SiO_2-$CaSO_4$-$CaCO_3$-H_2O. Cem. Concr. Res. 37(10):1379-1410. https://doi.org/10.1016/j.cemconres.2007.06.002.
38. Hyvert N, Sellier A, Duprat F, Rougeau P, Francisco P. 2010. Dependency of C–S–H carbonation rate on CO_2 pressure to explain transition from accelerated tests to natural carbonation. Cem. Concr. Res. 40(11):1582–1589. https://doi.org/10.1016/j.cemconres.2010.06.010.
39. Šavija B, Luković M. 2016. Carbonation of cement paste: Understanding, challenges, and opportunities. Constr. Build. Mater. 117:285–301. https://doi.org/10.1016/j.conbuildmat.2016.04.138.
40. Black L, Breen C, Yarwood J, Garbev K, Stemmermann P, Gasharova B. 2007. Structural features of C–S–H(I) and its carbonation in air—a raman spectroscopic study. Part II: Carbonated Phases. J. Am. Ceram. Soc. 90(3):908–917. https://doi.org/10.1111/j.1551-2916.2006.01429.x.
41. Arandigoyen M, Bicer-Simsir B, Alvarez JI, Lange DA. 2006. Variation of microstructure with carbonation in lime and blended pastes. Appl. Surf. Sci. 252(20):7562–7571. https://doi.org/10.1016/j.apsusc.2005.09.007.
42. Horgnies M, Chen JJ, Bouillon C. 2013. Overview about the use of fourier transform infrared spectroscopy to study cementitious materials, in: Brebbia CA, Klemm A (Eds.). Materials Characterisation VI Computational Methods and Experiments, Vol. 77, WIT Transactions on Engineering Sciences, WITPress, 77:251–262. https://doi.org/10.2495/MC130221.
43. Yan Y, Bernard E, Miron GD, Rentsch D, Ma B, Scrivener K, Lothenbach B. 2023. Kinetics of Al uptake in synthetic calcium silicate hydrate (C-S-H). Cem. Concr. Res. 172:107250. https://doi.org/10.1016/j.cemconres.2023.107250.
44. L'Hôpital E, Lothenbach B, Kulik DA, Scrivener K. 2016. Influence of calcium to silica ratio on aluminium uptake in calcium silicate hydrate. Cem. Concr. Res. 85:111-121. https://doi.org/10.1016/j.cemconres.2016.01.014.
45. Napia C, Sinsiri T, Jaturapitakkul C, Chindaprasirt P. 2012. Leaching of heavy metals from solidified waste using Portland cement and zeolite as a binder. Waste Manag. 32(7):1459-1467. https://doi.org/10.1016/j.wasman.2012.02.011.
46. Sugranez R, Alvarez JI, Cruz-Yusta M, Marmol I, Morales J, Sanchez L. 2013. Controlling the microstructure in cement based mortars by adjusting the particle size distribution of the raw materials. Constr. Build. Mater. 41:139-145. https://doi.org/10.1016/j.conbuildmat.2012.11.090.
47. Lawrence RM, Mays T., Rigby SP, Walker P, D'Ayala D. 2007. Effects of carbonation on the pore structure of non-hydraulic lime mortars, Cem. Con. Res. 37(7):1059–1069. https://doi.org/10.1016/j.cemconres.2007.04.011.
48. Raoof A, Nick HM, Wolterbeek TKT, Spiers CJ. 2012. Pore-scale modeling of reactive transport in wellbore cement under CO2 storage conditions. Int. J. Greenh. Gas Control. 11(S):S67–S77. https://doi.org/10.1016/j.ijggc.2012.09.012.
49. Morandeau A, Thiéry M, Dangla P. 2015. Impact of accelerated carbonation on OPC cement paste blended with fly ash. Cem. Concr. Res. 67:226–236. https://doi.org/10.1016/j.cemconres.2014.10.003.
50. Leemann A, Nygaard P, Kaufmann J, Loser L, Relation between carbonation resistance, mix design and exposure of mortar and concrete. Cem. Concr. Compos. 62:33–43. https://doi.org/10.1016/j.cemconcomp.2015.04.020.